

# Moisture-induced damage evolution in laminated beech

## Journal Article

**Author(s):**

Hassani, Mohammad Masoud; [Wittel, Falk K.](#) ; Ammann, Samuel; [Niemz, Peter](#) ; Herrmann, Hans J.

**Publication date:**

2016-09

**Permanent link:**

<https://doi.org/10.3929/ethz-b-000114941>

**Rights / license:**

[In Copyright - Non-Commercial Use Permitted](#)

**Originally published in:**

Wood Science and Technology 50(5), <https://doi.org/10.1007/s00226-016-0821-5>

# Moisture-induced damage evolution in laminated beech

Mohammad Masoud Hassani<sup>1</sup> · Falk K. Wittel<sup>1</sup> ·  
Samuel Ammann<sup>1</sup> · Peter Niemz<sup>1</sup> · Hans J. Herrmann<sup>1</sup>

Received: 12 March 2015 / Published online: 2 April 2016  
© Springer-Verlag Berlin Heidelberg 2016

**Abstract** In a combined experimental, numerical, and analytical approach, damage onset and propagation in unidirectional and cross-laminated samples from European beech due to climatic changes are studied. The inter- and intra-laminar damage evolution is characterized for various configurations, adhesively bonded by three structural adhesive systems. Different lamella thicknesses are studied to capture size effects. Typical situations are simulated by means of a comprehensive moisture-dependent nonlinear rheological finite element model for wood with the capability to capture delaminations. The simulations give insight into the role of different strain components such as viscoelastic, mechano-sorptive, plastic, and hygro-elastic deformations under changing moisture content in progressive damage and delamination. The stress buildup under cyclic hygric loading was shown, resulting in hygro-fatigue. It was demonstrated that a modified analytical micro-mechanics of damage model, originally developed for cross-ply laminates, can be employed to describe the problem of moisture-induced damage in beech lamellae.

## Introduction

New innovative timber engineering applications harness the improved mechanical performance of hardwood. High stiffness and strength of beech, for example, make it possible to achieve comparably slender, wide-spanning structures with respect to softwood. However, the disadvantageously low dimensional stability and inhomogeneity of beech make it necessary to adhesively bond smaller-sized pieces to form large laminated structural members. After several years of intense research on

---

✉ Falk K. Wittel  
fwittel@ethz.ch

<sup>1</sup> Institute for Building Materials, Department of Civil, Environmental and Geomatic Engineering, ETH Zurich, Stefano-Franscini Platz 3, 8093 Zurich, Switzerland

adhesive bonding of hardwood, it becomes evident that the traditional framework, manifested in codes for adhesive bonding of softwood, is hardly applicable to hardwood (Ammann et al. 2016). Typically, for beam or plate structures, the longitudinal axes (L) of lamellae are oriented coaxially or perpendicularly to each other. Climatic changes or moisture gradients can result in high residual stresses that often exceed the values of the yield stress or strength of bulk wood and adhesive bonding alike. Moreover, in real structures, different moisture contents of components prior to gluing can significantly contribute to the development of residual stresses. Consequently, various types of inter- and intra-laminar cracks form, which are defined by the normal orientation of the crack plane and the corresponding propagation direction. The weakest crack systems in wood are commonly TL, RL, and TR; thus, crack planes with the normal directions in the tangential (T) and radial (R) direction (first letter) propagate along the grain (L) or in the radial direction (second letter) (Wittel et al. 2005; Silva et al. 2006; Fortino et al. 2012; Qiu et al. 2014).

Adhesive bond lines can be considered as internal interfaces with distinct properties from adherends and adhesives and strong gradients in material behavior (Hass et al. 2012a). Cracks can penetrate adhesive bond lines or can be deflected into it what results in delaminations. This is determined by mechanical performance of the bond line due to adhesive, cohesive, or interphase fracture (Serrano 2000; Simon and Valentin 2003; Fortino et al. 2012; Hass et al. 2013). The conditions that lead to damage and its propagation cannot be understood, if the available energy for crack formation is not known. Unfortunately, experiments alone will not be able to provide this insight as the observed deformations are a combination of reversible hygro-elastic, irreversible plastic and history-dependent viscoelastic and mechano-sorptive strain components. To make matter worse, most constitutive parameters of wood and adhesives exhibit significant nonlinear dependence on the moisture content rendering intuitive explanations questionable (Hering 2011). However, numerical simulations, e.g., with finite element methods (FEM), can cope with the arising complexity of the coupled hygro-mechanical problem. Since they are based on continuum assumptions, effects of disorder—present on all hierarchical scales of wood—are smeared out. One obtains so to say the average answer over many components or samples. Even though results might not correspond to an individual, specific sample, the much more important general behavior as well as physical insight are provided by the simulations.

In this manuscript, the damage evolution is studied in small, three-layered beech wood panels of various thicknesses, adhesively laminated in aligned or crosswise way by three structural adhesives with distinct mechanical behavior based on a combined experimental, numerical, and analytical approach. Intra- and inter-laminar damage develop and evolve above a certain thickness as freely supported samples cycle through drying and moistening conditions. Furthermore, analogy is made to the well-studied problem of progressive transverse ply cracking in cross-ply composite laminates (Wittel et al. 2003), and the experimental observations are interpreted for cross-laminated wood elements in the energy-based micro-mechanics of damage framework (Nairn 1989; Liu and Nairn 1990; Nairn and Hu 1992). Since this method has been considered as a standard in composite design for at least

two decades, it is referred to the review articles in Nairn and Hu (1994) for a detailed description. Unfortunately, this approach is limited to linear hygro(thermo)-elastic, transversely isotropic material bodies. To capture the complicated moisture-dependent rheology of wood, however, advanced material models are required, like the recently introduced model that combines moisture-mechanical simulations with a hygro-elastic material including multi-surface plasticity, linear viscoelasticity, and mechano-sorption, all considering directional and moisture-dependent parameters (Hassani et al. 2015). Only if one does not neglect the relevant rheonomous and scleronomous strain portions that contribute to the total strain, local stresses and strain energy densities can be calculated correctly and failure criteria can be used to make correct predictions. With this approach, the important problem of hygro-fatigue that is puzzling timber engineers in the form of spontaneous structural failures, even decades after erection, naturally emerges by the sequential stress buildup.

This paper is organized as follows: In the Materials and Methods section, a detailed description of the experimental campaign is given followed by a brief introduction of the rheological models. Model parameters that were not fully described in Hassani et al. (2015), however, are summarized in the Materials and Methods section. In the Results section, the experimental observations on various configurations after the first two moisture cycles are first discussed. The damage evolution is characterized by typical properties common to the intra- and inter-laminar fracture studies. FEM simulations are simulated on the macroscopic behavior of a set of experiments, before the model is applied to gain deeper insight into the mechanical situation that leads to the observed damage evolution. Hence, cracks in the middle lamella are first artificially introduced, and then, the change in the strain fields and stresses for the onset of delamination as well as its propagation are calculated using fracture mechanics. As the experimental time frame is limited to two cycles only, it is extended by simulations to ten cycles (3 years) to be able to quantify the stress buildup for longer moisture histories. These simulations are very detailed with respect to the material behavior. To be able to make more general statements on the damage evolution and scaling, a variational mechanical approach to the moisture-induced damage evolution studied in this manuscript is adopted. Finally, we conclude on the applicability of this study to delamination testing of adhesive systems.

## Materials and methods

### Experimental tests

Three-layered European beech samples of various configurations were produced to undergo cyclic climatic changes. All samples had dimensions of  $L = 100 \text{ mm} \times 100 \text{ mm}$ , but different thicknesses of  $2d$  with  $d = 4, 10, 20, 30 \text{ mm}$  being named T1 to T4, respectively. They were either glued with parallel grain (P1) or crosswise (P2) with the L-direction of the middle lamella of thickness  $d$  being perpendicular to the ones of the outer layers with thickness  $d/2$  each (see

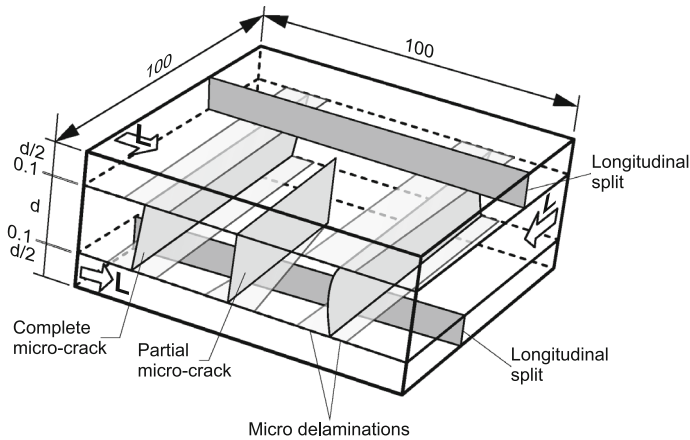


**Fig. 1** Cross-laminated sample with dimensions in millimeter and different kinds of failure mechanisms

Fig. 1). For adhesive bonding, three commonly used adhesive systems in timber construction, namely melamine urea formaldehyde (MUF, Kauramin 683: hardener 688 = 100 g:20 g), phenol resorcinol formaldehyde (PRF, Aerodux 185 RL: hardener HP 155 = 100 g:20 g), and one-component polyurethane (1C PUR, Purbond HBS 709) were applied. The amount of adhesive applied was 340–440 g/m<sup>2</sup> on one side for MUF, 225 g/m<sup>2</sup> on each side for PRF, and 180 g/m<sup>2</sup> on one side for PUR with respective pressing times in hours of 18.5 (MUF), 4 (PRF), and 3 (PUR). The wood was conditioned and glued at 20 °C/95 % relative humidity (RH). To avoid drying during cold curing in the press machine under 1.2 MPa, samples were sealed from the environment by wrapping them in foil. For each configuration T1–T4, P1–P2 and adhesive type MUF–PRF–PUR, four samples were produced, resulting in 90 samples for testing. Just to give an example, sample P2-PUR-T3-2 refers to the second cross-laminated sample with 20 mm thick middle lamella glued by PUR adhesive. Note that bonding with MUF and PRF at 20 °C/95 % RH can result in starved bond lines, while PUR performs outstandingly when bonded under wet conditions. Nevertheless, in the current study, this approach for the model experiments was chosen to obtain strong tensile stresses upon drying.

All samples were placed in internally ventilated climate boxes for drying and re-moistening. A moisture cycle comprised the following steps: (a) de-moistening from a nearly fiber saturated condition (95 % RH) to 2 % RH (resulting in a wood MC of about 2.4 %), (b) re-moistening to 95 % RH. Drying was established using a layer of silica gel and re-moistening by vaporized distilled water. RH was recorded by means of a RH recorder located in each box. When the mass change was below 0.1 %/day, the samples were considered to be equilibrated with the climate inside the box. At the end of every drying stage, the moisture-induced dimensional changes and deformations were recorded using a dial gauge. The climatic changes resulted in a change in moisture content of approximately 20 %. Due to differences in the shrinkage behavior of adjacent layers, micro-cracks and delaminations were expected to form (see Fig. 1). The initiation and evolution of the inter- and intra-

laminar cracks were recorded by scanning each side of every laminated sample with a flatbed scanner for further evaluation.

## Numerical procedure

For a better interpretation, a 3D orthotropic moisture-dependent constitutive material model for wood was used consisting of all instantaneous and history-dependent responses, namely hygro-elastic (el), plastic (pl), viscoelastic (ve), and mechano-sorptive (ms) deformation modes, previously developed and validated. For a full description of the implementation in the FEM package ABAQUS along with parameters used for beech, it is referred to Hassani et al. (2015). The model gives for the first time the possibility to attain a better quantitative understanding of the true distribution and evolution of the moisture-induced stresses as the main driving forces for the formation of inter- and intra-laminar fracture. Note that the moisture analysis is only sequentially coupled with the nonlinear mechanical analysis. The presence of adhesive bond lines requires special treatment with respect to moisture transport and mechanical behavior.

In principle, a simplified moisture-dependent material model compared to the one used for wood was employed for adhesives. In case of PRF, it was a simple isotropic, hygro-elastic model; for MUF, viscoelasticity was added, and for PUR, plasticity was added, represented by the simple J2-plasticity with isotropic hardening. A complete set of moisture-dependent adhesive properties for MUF, PRF, and PUR is given in Table 1. Hence, in combination with the full model description in Hassani et al. (2015), all required parameters are defined.

The five-layered FEM model consists of three solid wood lamellae and two adhesive layers. Cohesive elements connect the adhesives with the middle layer to allow for the simulation of the onset and evolution of delamination within the framework of nonlinear fracture mechanics (Alfano and Crisfield 2001; de Borst et al. 2004). The cohesive zone models were characterized in terms of the so-called traction–separation relationships describing the damage initiation and evolution laws. In the current study, the COH3D8 8-node 3D cohesive elements of ABAQUS (2014) with an uncoupled traction–separation approach were used. Delaminations were initiated due to a maximum nominal stress criterion followed by an energy-based damage evolution law with exponential softening. Mixed-mode cases were considered by a power law interaction criterion with the exponent of 1.6 taken from Fortino et al. (2012). Table 2 summarizes all cohesive parameters utilized to characterize the fracture process zone. The adhesive bond line was modeled by volume elements of thickness 0.1 mm, while a thickness of 0.001 mm was assigned to the cohesive layer. ABAQUS by default uses the constitutive thickness equal to unity in the calculations. To capture the influence of the geometrical thickness, the normal and shear stiffness of the cohesive elements, representing the slope of the linear part of the traction–separation laws, was normalized by the actual thickness (see Table 2). Note that only average values of the adhesive moisture-dependent Young's and shear moduli in a range from 0 to 5 % moisture content were considered, since the dry state is the critical one with respect to the delamination growth. For wood layers with significant curvature of the growth rings

**Table 1** Material model parameters for MUF, PRF, and PUR adhesives

Coefficients for calculation of moisture-dependent Young's modulus for different adhesive systems fitted to the data published in Kläusler et al. (2013). The value of the Poisson's ratio for all adhesive types is taken as  $\nu_{\text{adh}} = 0.3$

	$a_0$ (MPa)	$a_1$ (MPa/%mc)	$a_2$ (MPa/%mc <sup>2</sup> )	$a_3$ (MPa/%mc <sup>3</sup> )
$E_{\text{adh}}(\omega) = a_0 + a_1\omega + a_2\omega^2 + a_3\omega^3$				
MUF	5355.0	−604.100	33.270	−0.6805
PRF	4176.0	−176.90	19.38	−0.8521
PUR	1242.0	−158.300	26.250	−6.443

Moisture expansion coefficients (CME) of different generic adhesive types given in Zhang et al. (2005)

CME	$\beta$ (1/%mc)
MUF	0.00198063
PRF	0.00172869
PUR	0.00171628

Normal entries of the viscoelastic compliance tensor  $J_i$  pertaining to a serial association of six Kelvin–Voigt elements for different adhesive systems identified in Touati and Cederbaum (1997a, b).  $\tau_i$  designates the characteristic retardation time relevant to the  $i$ th Kelvin–Voigt element

$i$ (–)	$\tau_i$ (h)	MUF $J_i$ (TPa <sup>−1</sup> )	PUR $J_i$ (TPa <sup>−1</sup> )
1	1E-4	1.94658	4.63471
2	1E-3	0.75542	1.79861
3	1E-2	1.13317	2.69802
4	1E-1	1.40612	3.34791
5	1E0	2.59639	6.18187
6	1E1	1.00645	2.39631

Coefficients for calculation of moisture-dependent strength value  $S_y(\omega)$  and nonlinear hardening stress function  $q(\omega)$  for PUR adhesive fitted to the data published in Kläusler et al. (2013).  $\omega$  and  $\alpha$  denote the MC and strain-type internal state variable, respectively

$b_0$ (MPa)	$b_1$ (MPa/%mc)	$b_2$ (MPa/%mc <sup>2</sup> )	$b_3$ (MPa /%mc <sup>3</sup> )
$S_y(\omega) = b_0 + b_1\omega + b_2\omega^2 + b_3\omega^3$			
29.21	−7.734	4.696	−0.9505

$C_0$ (MPa)	$C_1$ (MPa/%mc)	$C_2$ (–)
$q(\omega) = (C_0 + C_1\omega)\alpha^{C_2}$		
60.3030	−12.1352	0.5326

Parameters for the calculation of moisture-dependent diffusion coefficients for different adhesive systems following Volkmer et al. (2012) and Wimmer et al. (2013)

	$D_0$ (mm <sup>2</sup> /h)	$\alpha_0$ (–)
$D(\omega) = D_0e^{\alpha_0\omega}$		
MUF	9.792E-04	0.231
PRF	4.047E-04	0.231
PUR	3.067E-03	0.057

**Table 2** Parameters for the nonlinear traction–separation behavior of the cohesive element for PUR

$T_{nn}$ (MPa)	$T_{ss}$ (MPa)	$T_{tt}$ (MPa)
Damage initiation parameters Serrano (2000)		
6.55	14.2	14.2
$G_I$ (N/mm)	$G_{II}$ (N/mm)	$G_{III}$ (N/mm)
Damage evolution parameters/fracture energies Serrano (2004)		
0.75	1.45	1.45
$K_{nn}$ (MPa)	$K_{ss}$ (MPa)	$K_{tt}$ (MPa)
Stiffness values		
1,157,900	445,400	445,400

( $d > 10$  mm), the material orthotropy was assigned in a cylindrical coordinate system by estimating the location of the center (pith) from the local curvatures of each layer obtained from the side scans.

The only change in the boundary conditions of the simulations was the moisture content applied to all external faces of the model. The relation to the experimentally measured RH is given by the sorption isotherm curves for solid wood and all adhesive types (Wimmer et al. 2013). It is assumed that moisture transport inside the system can be described by Fick's law (Fortino et al. 2009; Gereke 2009). The obtained moisture field evolution is used in the subsequent stress analysis with the nonlinear material models. One obtains full access now to all relevant strain components and resulting stresses. To allow for simple generation of each individual sample with its respective material coordinate systems, a parameterized script-based approach was chosen. A typical model is shown in Fig. 2. Note that with the approach described, degradation planes can only be artificially introduced in the middle lamella at experimentally observed positions, and subsequently, the evolution of the strain fields as well as delamination initiation and propagation is calculated. In principle, one can extend the material model with capabilities for softening under tension or shear to localize micro-cracks.

### Analytical approach to damage evolution

In the analytical approach, it was attempted to adopt a much more general fracture mechanical model that is not limited by system sizes and is capable of predicting size effects in the damage evolution. The most suitable analytical solution to the damage in cross-laminated samples is given by micro-mechanics of damage approach, developed and reviewed by Nairn and Hu (1992, 1994). It consists of two steps: (a) the use of micro-mechanics to analyze the stress field in a composite in the presence of damage, determining the unit cell by its limiting cracks (the unit cell of damage is defined as the region between two adjacent micro-cracks, see Fig. 10 inset) and (b) the use of a failure criterion to predict the evolution of damage. The



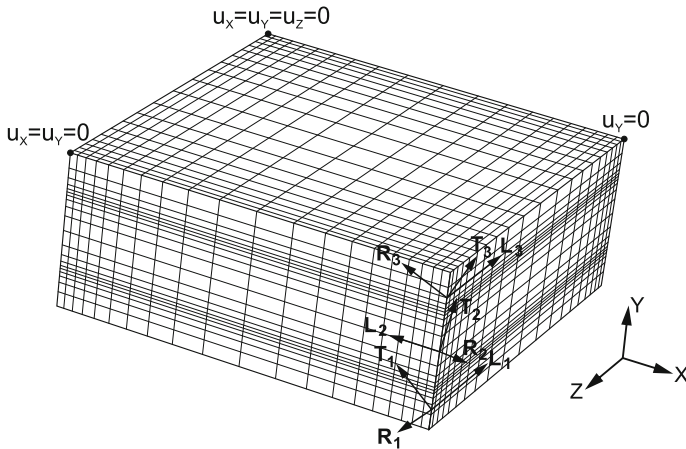


**Fig. 2** Exemplary FEM model with applied boundary conditions and local material coordinate systems consisting of twenty-node quadratic brick elements with reduced integration (C3D20R) and linear cohesive elements (COH3D8)

equations for calculating the stress field in the two-dimensional (2D) unit cell are derived from variational mechanics. For high stiffness contrast of adjacent lamellae, like in the case of beech ( $E_{LL}/E_{RR}$ ), the sample edges can limit the unit cell.

The process is driven under drying in analogy to thermal cycling by differences in the hygro-expansion of the lamellae. Energy can be dissipated either by the formation of new micro-cracks, increasing the crack density, or by the initiation of delaminations at the tips of existing micro-cracks. This is expressed by the competition between the respective energy release rates (ERR)  $G_{mc}$  and  $G_{dc}$  for intra- and inter-laminar failure. Once  $G_{dc}$  dominates  $G_{mc}$ , micro-delaminations form and the saturation crack density is reached, only allowing further energy dissipation by delamination growth. The model predicts the stress states in the middle as well as the ones in the outer lamellae, resulting in their cracking and delamination from the middle lamella under drying as well (Fig. 16). For simplification, the material is considered as transversely orthotropic, linear elastic with properties that correspond to the dry state ( $MC \approx 2.4\%$ ).

## Results

On a micro-mechanical scale, crack formation can be interpreted either as fiber cell wall failure or as fiber de-bonding (Wittel et al. 2005). In principle, crack propagation by de-bonding consumes less energy, but is bound to fixed degradation planes, originating from the cellular arrangements. The large content of ray tissue of beech and the huge porosity due to the intra-ring vessel network (Hass et al. 2010) result in additional micro-mechanical damage mechanisms. In this study, however, cracks are addressed as if they would grow in a homogeneous, anisotropic medium. The expected types of intra-laminar failure are straight or curved RT or TL

transverse micro-cracks that partially or entirely split the middle or outer lamellae. At the bond line, cracks become inter-laminar by penetrating the bond line or by being deflected along the interface resulting in delaminations, whatever mechanism is energetically favorable. A summary of the expected fracture types is sketched in Fig. 1.

## Experimental observations

### *Samples with coaxial L-directions (P1)*

Lamellae with aligned grain orientations are typically found in structural glulam beams. Transverse cracks are usually not problematic, but micro-delaminations from crack deflections into the interface significantly disturb the shear coupling of adjacent lamellae, weakening the entire element in terms of strength and stiffness. To reduce cracking, lamella thicknesses are limited by design codes and longitudinal stress relief cuts are often introduced.

Thin samples with a middle lamella thickness of  $d = 4$  mm (P1-MUF/PRF/PUR-T1) showed no sign of damage, but an excessive warping deformation that even increased in consecutive cycles. The dependence of the maximum warping deflection ( $u_w$ ) on the adhesive type and middle lamella thickness  $d$  is shown in Fig. 3. The moisture-induced deformations accumulate when cycling, resulting in hygro-fatigue. Further, the accumulated magnitude of the moisture-induced warping

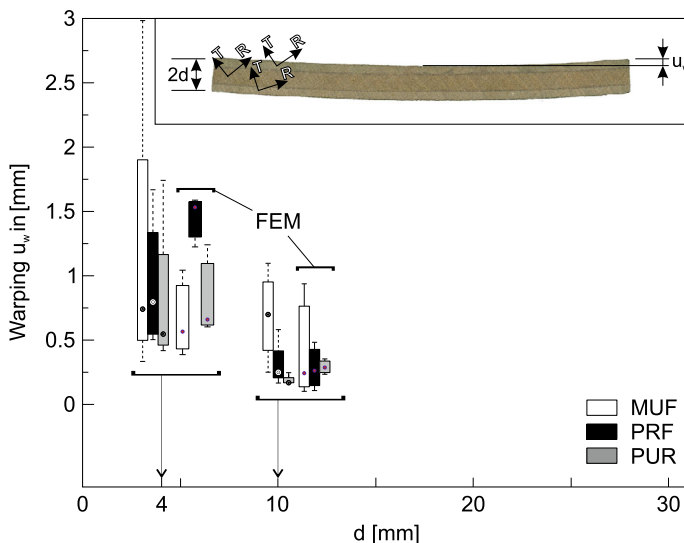


**Fig. 3** Dependence of the maximum warping deflection ( $u_w$ ) on the adhesive type and middle lamella thickness  $d$  averaged over three samples. Note that the central box indicates the central 50 % of a data set (limited by the lower and upper boundaries representing the 25 % and 75 % quantile of data). The central point shows the median, and the dashed lines connect the upper and lower markers for data outside of the central box. The inset gives a side view of the deformed shape of the P1-PUR-T1-4 sample at the end of the second de-moistening step

depends on the mechanical performance of the adhesive type in the order of MUF–PRF–PUR, what corresponds to the respective order of stiffness (see Table 1). The stiffest bond line, therefore, has more hindering ability and lessens the deformation.

For all aligned samples with the middle lamella thickness  $d = 10$  mm (P1-MUF/PRF/PUR-T2), no damage was recorded at the end of the first drying step. P1-MUF/PUR-T2 samples remained flawless, even after the second de-moistening, while few TL-cracks appeared in the middle lamella of T2 samples laminated with PRF adhesive, pointing at the importance of the relative orientation of the longitudinally aligned lamellae material coordinate systems.

For thicker samples with  $d = 20$  mm and  $d = 30$  mm (P1-T3/T4), mainly all middle lamellae cracked with the TL crack system, primarily during the first de-moistening. In the second drying step, those cracks mostly propagated toward the bond lines (TR growth system). When reaching it, three different scenarios were observed: (a) crack arrest at the interface, (b) crack penetration through the bond line and further propagation, (c) deflection into the interface (see Fig. 4). In principle, cracks propagate along the path that minimizes the energy (He et al. 1994). Herein, the anatomic orientations of wood lamellae are a key issue if the stress enhancement at the crack tip is not weakened by a very soft interface. From Fig. 4, it can be realized that when the weak TL planes of adjacent laminates are similar, cracks simply penetrate the interface, whereas for strongly different  $T$ -axes, it can be more favorable for cracks to be deflected and to grow along the bond line, depending on the adhesive type. This results in micro-delaminations or—if bond lines are tough—in bond line penetration, followed by crack growth along paths that are more energy consuming with respect to the growth in the fixed degradation plane of the TL-cracks. Note that changes in the growth direction into the weak TL growth system were also observed at later stages.

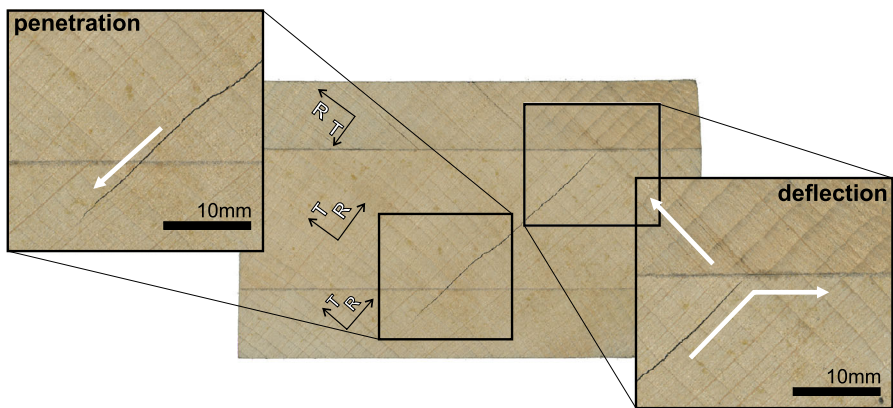


**Fig. 4** End grain surface views of the P1-PUR-T4-1 sample after the second drying, illustrating the deflected and penetrating cracks. Arrows mark the propagation trajectory after intersection with the interface

### Samples with crossed L-directions (P2)

Similar to the aligned ones, none of the T1 samples with  $d = 4$  mm showed any observable damage. As expected, the warping was significantly reduced in the crosswise configurations with odd number of layers (balanced laminates). However, the increased dimensional stability resulted in stronger edge face deformations ( $u_{sw}$  in Fig. 5) due to larger residual stresses in crosswise patterns. One can observe a similar dependence of the side warping on the adhesive stiffness as for the warping deflection of the aligned samples.

With increasing thickness  $d$ , stresses due to drying exceeded strength values. For  $d = 4$  mm (T1), no damage was observed, while in  $d = 10$  mm (T2) samples, inter- and intra-laminar failure developed regardless of the material orientation and adhesive type. Figure 6 shows the edge views of a sample (P2-MUF-T2-2) for two successive de-moistening stages. After the first de-moistening (left), an approximately evenly spaced set of inclined micro-cracks is observed. The quasiperiodicity is the result of a process where cracks form sequentially between existing cracks in accordance with transverse ply cracking in cross-ply laminates (Nairn 1989; Liu and

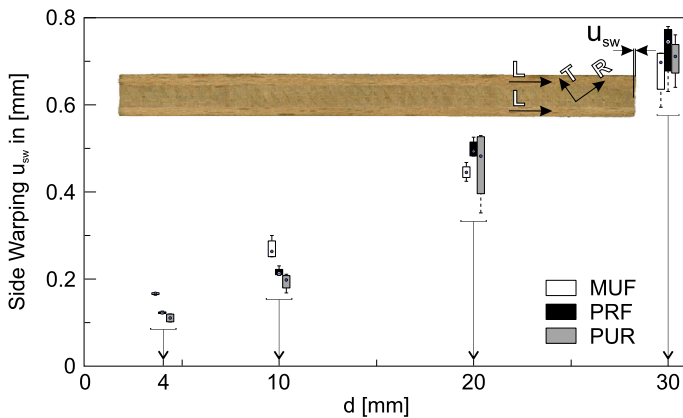


**Fig. 5** Side warping ( $u_{sw}$ ) of all P2 samples after the first de-moistening step. *Inset* sample P2-MUF-T1-2 at the end of the second de-moistening stage



**Fig. 6** Side views of the fractured P2-MUF-T2-2 sample after the first (*left*) and the second (*right*) de-moistening steps, displaying the formation of equally distanced curved micro-cracks that span the entire sample width and micro-crack-induced de-bonding

Nairn 1990; Nairn and Hu 1992, 1994). As stresses in the middle layer are introduced by shear at the layer interfaces, they exhibit shear lag in a spatially limited zone. If the shear lag zone is smaller than the half crack spacing, an unperturbed zone exists where new cracks can initiate at the weakest location. If the shear lag zones interfere, new cracks primarily form between existing cracks where the stress is maximal. In the second de-moistening, no further transverse cracks formed, but micro-crack-induced delaminations emanated from all micro-crack tips. Since no shear stress can be transmitted through the delaminations, the shear lag zones became closer, and consequently, the saturation crack density was reached (Nairn and Hu 1994).

The damage of the outer layers is best visible when the sample is rotated. It is characterized by a staggered or antisymmetric pattern of micro-cracks and adhesive failure (see Fig. 6). In the second drying phase, a new micro-crack initiated in a non-symmetric manner and additionally further de-bonding, originating from the micro-crack tips and edges, formed. Samples with PUR and PRF adhesives behaved similar to MUF-glued samples, but exhibited a smaller crack density in general. These observations are in agreement with typical crack formation processes in cross-ply laminates driven by a contrast in the Poisson's ratios and expansion coefficients of adjacent layers (Nairn and Hu 1992, 1994). Like for MUF samples, the crack opening increased in the second moisture cycle, pointing at the importance of the irreversible strains. It is interesting to note that cracks can be inclined since the formation of a longer crack along the weak TL plane can be energetically advantageous compared to a perpendicular crack which is shorter, but requires more energy to grow.

The general fracture behavior of P2-T3 samples ( $d = 20$  mm) was identical with their P2-T2 counterparts with the same adhesive system. The damage evolution is shown for the P2-PRF-T3-2 sample in Fig. 7. Note that regardless of the TL degradation plane, two more or less regularly spaced partially straight transverse micro-cracks formed as well as a *top layer* crack with delamination

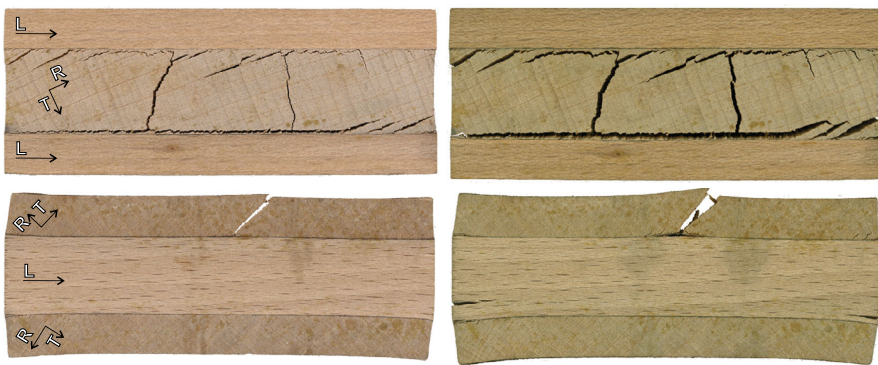


**Fig. 7** Side views of the fractured P2-PRF-T3-2 sample after the first (*left*) and the second (*right*) de-moistening steps with a pair of relatively straight transverse micro-cracks formed as well as a *top layer* crack with delamination





**Fig. 8** Side views of the fractured P2-PUR-T4-1 sample after the first (*left*) and the second (*right*) de-moistening steps with a single straight transverse micro-crack and severe intra-laminar TL-cracking

As the middle lamella thickness increased to  $d = 30$  mm (P2-T4), the analogy to transverse ply cracking breaks down, since the crack spacing reached sample dimensions. Eventually, growth in the weak TL plane dominated, entirely splitting the middle lamella and thus avoiding further transverse crack formation (see Fig. 8). The curvature of the growth rings, hence the location of the pith, plays a crucial role for intra- and inter-laminar damage as it dominates the overall stress state from the restrained shrinkage.

#### *Observations on bond line performance*

The failure modes of the MUF and PRF/PUR bond lines were characterized differently by adhesive failure and interphase delamination, respectively. MUF bond lines predominantly exhibited adhesive failure for all thicknesses  $d$ . This is due to the high stiffness of the MUF resulting in a hard layer of the bulk adhesive incapable of reducing interfacial stresses. Moreover, the penetration of the MUF adhesive into the interphase layer increases the brittleness of the cellular structure and decreases the rigidity and the strength of the interface (Fortino et al. 2012). The superior performance of the PUR bond line with fracture toughness higher than adjoining hard substrates can be associated with the occurrence of the plastic deformations within the adhesive material leading to a more flexible interface with the ability of reducing stress concentrations (River 2003). Note that differences also originate from a distinct liquid adhesive penetration behavior into the vessel network (Hass et al. 2012b; Mendoza et al. 2012). Hence, under identical situations, the delamination is less pronounced (see Fig. 9). Similarly, the rigidity and the



**Fig. 9** P2-X-T3 samples ( $d = 20$  mm) with different adhesives after the first de-moistening exhibiting adhesive failure in the MUF and interphase failure in the PRF and PUR bond lines

endurance of the PRF bonded joints compared to the solid wood adherends can be attributed to the moderate stiffness and also the tendency of the PRF to receive more water resulting in a more plasticized and softer interface able to lower the stress concentrations all over the bond line (River 2003). Note that this study here shows similarities to delamination testing (DIN EN 14080 2013), addressing the requirements of European product standard for glued laminated timber with respect to delamination. However, the timescale of these experiments is in months, while DIN EN 14080 is in hours, using liquid water infiltration and drying ovens operating way above the room temperature. As a result, unpredictable effects of elevated temperature as well as artificial moisture gradient-induced damage propagation with respect to structural use of glued laminated timber have to be expected, in contrast to the approach proposed in this manuscript.

The damage state is best quantified by the micro-crack density and the delamination ratio defined as  $0.5(d_1 + d_2) \cdot a^{-1}$  (see Fig. 10). One can observe the tendency of increasing delamination ratios, but decreasing crack density with increasing thickness  $d$ .

### Numerical prediction of damage in cross-laminated samples under changing climate

As the moisture controls all hygro-mechanical properties, its gradients due to diffusive moisture transport as well as differential swelling are the main driving forces for the damage evolution in laminated wood. In the first step, the three-dimensional moisture fields were calculated, exhibiting large gradients across the lamellae interfaces (see Fig. 11). The simulation was repeated for all adhesives using sorptive transport properties from Volkmer et al. (2012) and Wimmer et al. (2013) fitted to the equation and parameters summarized in Table 1. The resulting moisture profiles for different adhesive systems are basically identical, showing the irrelevance of the diffusive transport through adhesives compared to the one in the solid wood.

The deflection of glued laminated panels under changing MC with the material models has already been calculated using the previously determined evolution of the

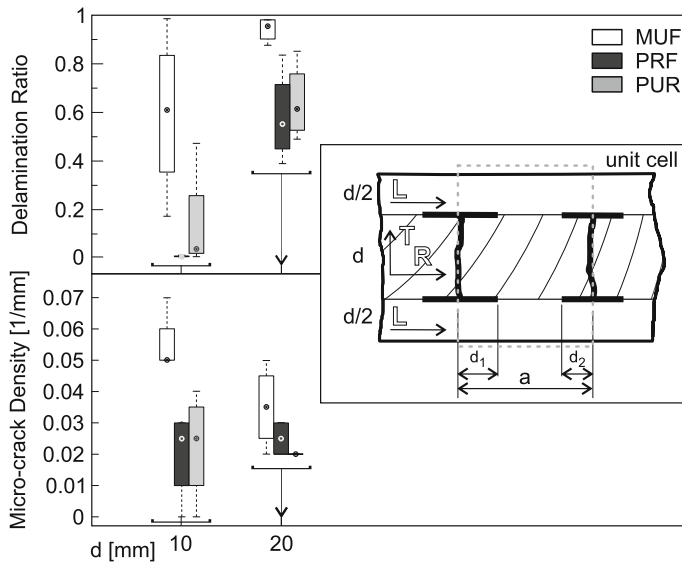


**Fig. 10** Damage states after the second drying for different thicknesses and adhesive types. The *inset* shows a sketch of the side view on the sample with the unit cell for the analytical stress calculation delimited by two adjacent micro-cracks with crack spacing  $a$  and respective micro-delaminations of length  $d_1$  and  $d_2$  (bold lines). Inclined lines in the middle lamella symbolize growth ring boundaries

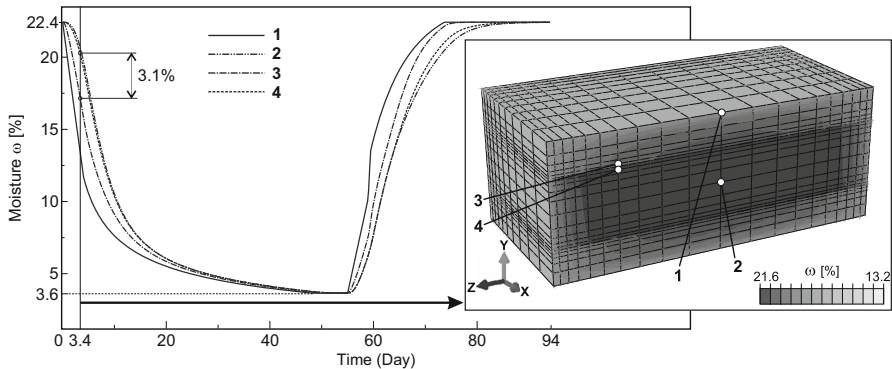


**Fig. 11** Moisture evolution at specific points and (*inset*) sectional view through center of the moisture field in the P2-T3-3 sample after 1.4 days

moisture field. This calculation was done for all coaxial T1/2 samples with their respective growth ring orientations. Good agreement is found with respect to the experimental values measured at the end of the second de-moistening step (see Fig. 3), even though material parameters are identical for all calculations, which is clearly not the case for the experiments. Note that further verification examples for the material model can be found in Hassani et al. (2015). In the following, the material models are applied to predict the influence of the total strain constituents on



the failure of cross-laminated configurations. To gain deeper insight into the damage onset and evolution, fracture mechanical simulations using the cohesive interface elements are performed.

Delaminations emanate from existing transverse cracks, before they initiate at free edges (see Fig. 14 right). This, however, does not mean that transverse cracks necessarily have to form before edge delaminations can occur. To understand the damage process, it is important to look at the situation for delamination initiation at a single crack. This case is simulated by artificially opening a crack at the dry state and then calculating a moistening and another de-moistening phase. It is striking to observe how the crack opening displacement (COD) of the transverse crack, which forms in the first drying phase, increases in the next step (see Fig. 12), driving

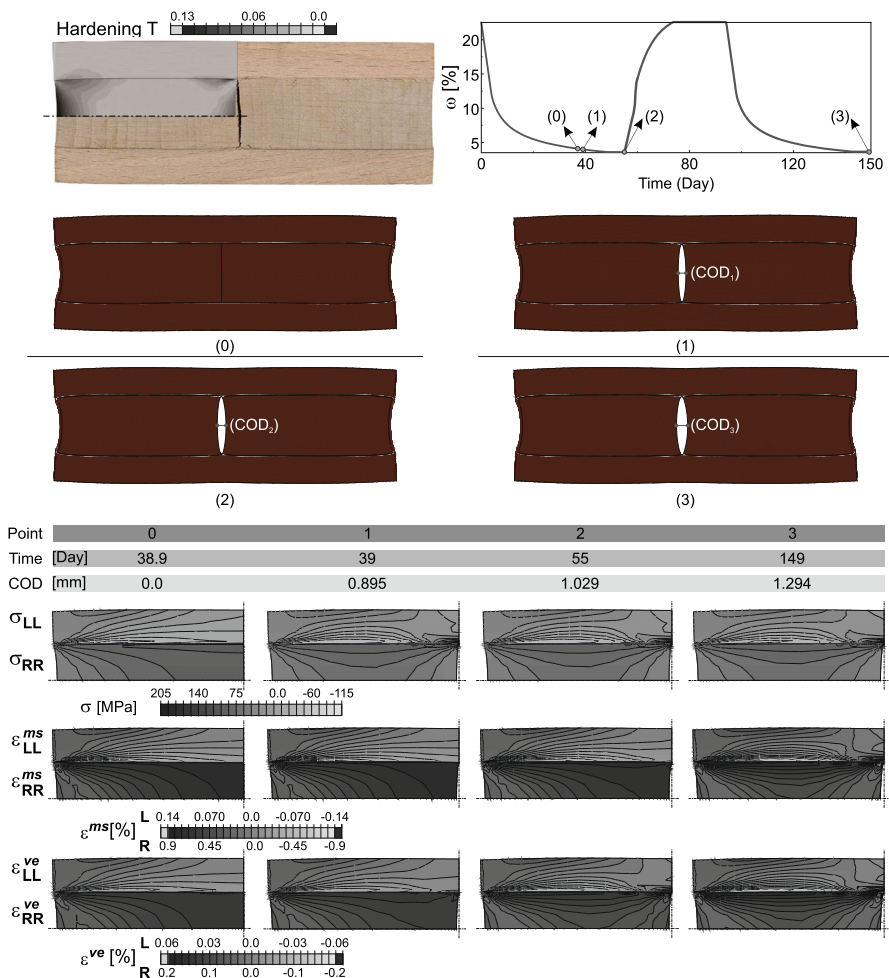


**Fig. 12** Strain evolution in quarter-models upon formation of a transverse crack with suppressed delamination for the P2-PUR-T3-3 sample with identical legends for the time evolution

micro-delaminations. When the crack forms, the elastic strains are immediately relaxed and the relaxation of the viscoelastic strains starts. This is true for the cracked middle layer as well as for the compressively loaded outer plies. However, this does not explain the increased COD in the consecutive cycles. Provided that no delaminations occur, the COD increases as visible in Fig. 12 by a decrease in the tensile mechano-sorptive strain during re-moistening, resulting in an increased COD of about 25 %. Additionally, as soon as the crack forms, the compressive plastic strains in the thickness directions develop (Fig. 12 top left in terms of the plastic hardening variable).

Delaminations can initiate and grow under different fracture modes like mode I opening and mode II shearing mode, most likely, however, as a mixture of both. To have a better understanding of how the middle layer cracking and adhesive type influence the distribution and value of interfacial stresses, the stress profiles with the components for mode I, the peeling stress ( $\sigma_{yy}$ ) and for mode II, the  $yz$  shear component ( $\sigma_{yz}$ ) are calculated along the edge (Path 1) and the center line (Path 2) of the lower adhesive bond line in the  $z$ -direction (see Fig. 13 right) after the second de-moistening step. The results show the effect of adhesive stiffness on the stress state (see Fig. 13 left). As it can be noticed, the distribution and amount of the shear components are more or less identical for all adhesive systems, while the magnitude of the normal stresses with similar distributions is inversely correlated with the order of adhesives stiffness (see Table 1).

Delaminations are much more severe than transverse cracks in terms of loss of stiffness of the laminate, as they result in large stress-free regions and significantly reduce the shear lag zones. Additionally, at the delamination fronts, the loading on the adhesive bond lines becomes maximal. The literature values for the critical ERR  $G_{IC}$  and  $G_{IIC}$  of adhesive bond lines in beech wood unfortunately are given with a substantial bandwidth. Therefore, a typical value used in Serrano (2004) is picked, and both modes are multiplied by a scalar multiplier.

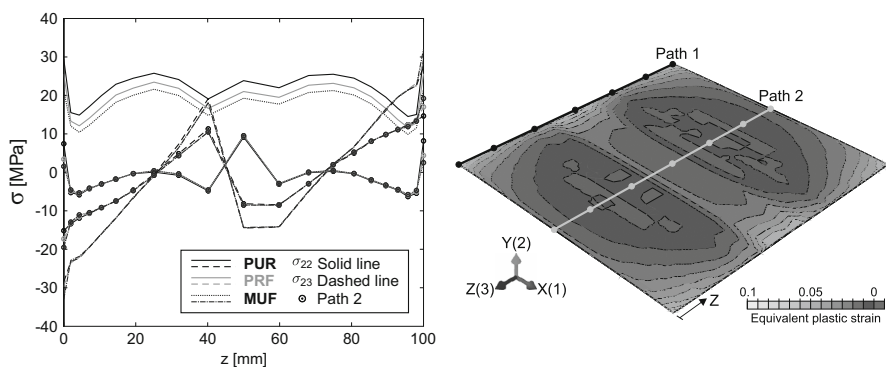


**Fig. 13** Peeling and shear stresses in the adhesive bond line along the Path 1 and Path 2 for different types of adhesive (*left*) and the equivalent plastic strain in the lower PUR adhesive layer (*right*) of the P2-T3 sample after the second de-moistening phase

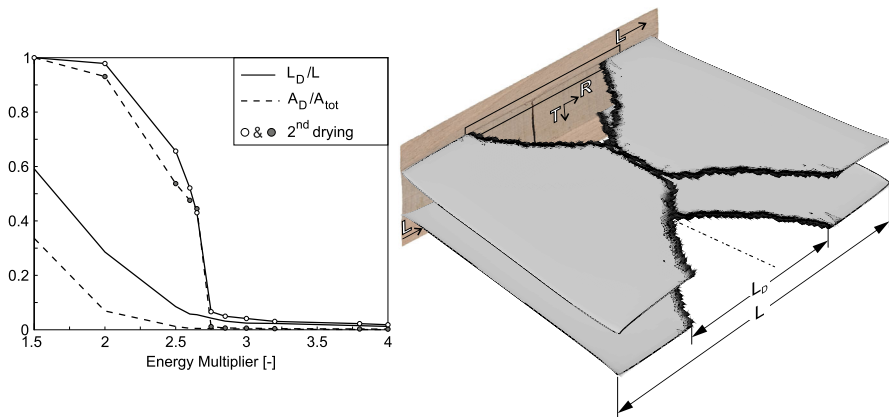


**Fig. 14** Relative delaminations ( $(A_D/A_{tot})$  and  $(L_D/L)$ ) versus the energy multiplier in the adhesive bond lines (left), and distribution of degradation scalar parameter (light gray intact, black almost delaminated, while delaminated elements are deleted) with delaminations for a multiplier value of 2.65 (right) compared to the P2-PUR-T3-3 sample

The calculated delamination ratio ( $A_D/A_{tot}$ ) and edge delamination length fraction ( $L_D/L$ ) for two successive cycles are shown as a function of the multiplier in Fig. 14 left. It is evident that delamination evolves in consecutive cycles with a concave delamination front (see Fig. 14 right). Note that due to the curvature, pure fracture modes are not present, pointing at the importance of mixed-mode criteria. In this case, the best agreement between the edge delamination length and the corresponding experimental observation (see Fig. 10) is obtained by setting the multiplier between 2.65 and 2.75 with respect to the values used in the linear elastic calculations (Serrano 2004), exhibiting the role of nonlinear energy dissipation at the delamination front.

Damage evolution was observed in the first two consecutive cycles experimentally, as well as in the calculations. Moisture gradients and swelling anisotropy both contribute to rather complicated stress states that relax by the buildup of the viscoelastic, mechano-sorptive or plastic strains. As a result, by inversion of the moisture content to the initial value, the sample does not return to the stress-free state, but can build up inverse stresses by the plastic deformation and mechano-sorption. To investigate the evolution of the stresses and different constituents of the total strain under cyclic hygric loading, ten moisture cycles were simulated, corresponding to 3 years, while experiments only captured two. This is demonstrated in two typical scenarios that both start at the stress-free condition, but case (I) is initially wet and then dries, while case (II) is initially dry and goes first through a moistening cycle. For clarity, only stresses and strains in the center point (point 2 in Fig. 11) in the radial direction with suppressed damage are visualized in Fig. 15.

*Case I* first dries, resulting in large tensile stresses that relax by the evolution of the viscoelastic and mechano-sorptive strains. When the sample is re-moistened, the stress state inverts, leading to the compressive stresses and dissipation by the

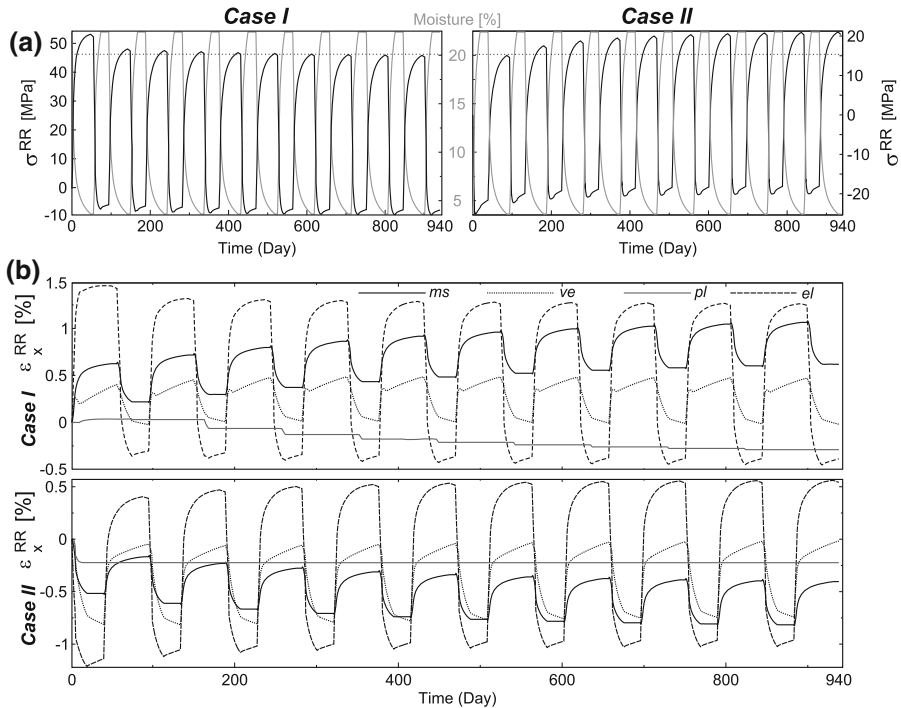


**Fig. 15** **a** Radial stress evolution in ten consecutive drying–moistening (case I, *left*) and moistening–drying (case II, *right*) cycles at the center of the P2-T3 sample (point 2 in Fig. 11) and **(b)** the evolution of different components of the total strain in drying–moistening (case I, *top*) and moistening–drying (case II, *bottom*) cycles (with identical legends). Subscript  $\times$  represents ms, ve, pl, or el for the respective strain components

plastic strains, as the moisture-dependent yield body shrinks due to moisture increase. In the consecutive moisture cycles, the added tensile stress due to the plastic strain increment is overcompensated by the increased viscoelastic strain and more importantly by the mechano-sorptive one. During every re-moistening phase, an additional but decreasing plastic strain increment is added (see Fig. 15b). In total, this causes a cyclic decrease in the maximum tensile stress that is becoming less significant after 5–6 cycles (see Fig. 15a).

*Case II* corresponds to adhesive bonding at rather dry states. When the sample is moistened for the first time, a significant plastic strain increment is formed while the central layer is in a compressive state. In re-drying, due to the expansion of yield surfaces, the inverted stresses cannot relax, resulting in significant tensile stresses. During consecutive cycles, the plastic strains remain constant, but mechano-sorptive and viscoelastic ones evolve (see Fig. 15b), leading to cyclic tensile stress accumulation upon re-drying that does exceed the strength values (see Fig. 15a). This can be considered as the driving mechanism behind hygro-fatigue.

## Analytical prediction of micro-cracking in cross-laminated samples

Simulating the damage evolution with the initiation and evolution of multiple cracks in different lamellae is still beyond the scope of a comprehensive FEM approach. However, the micro-mechanics of damage approach by Nairn and Hu (1992, 1994) can be employed with some limitations. A first micro-crack forms during the first drying in a region of more or less constant tensile stress  $\sigma_{xx}$ . As one can see in the resulting stress profiles (see Fig. 16), the material assumptions lead to stresses above known strength values. However, verification calculation with the FEM approach that only considers the hygro-elastic part of the wood material model gives rise to similar stress values. Hence, the analytical approach will have mainly qualitative character.

Nevertheless, the framework of micro-mechanics of damage helps in rationalizing the damage evolution. It is only during the second drying step that the strength of the middle lamella is overcome and segment II (in Fig. 16 T2 left) fractures, preferably in the mid-span, in the region of maximum tensile stress as predicted by the model resulting in  $N = 3$  segments. Since, micro-delaminations also form (see Fig. 16 T2 right),  $\rho^{10} = (N/L) = (3/100) = 0.03 \text{ mm}^{-1}$  is taken as the critical micro-crack density for this sample. Once  $\rho^{10}$  is known, the critical intra-laminar ERR ( $G_{mc}$ ) is determined and its relation with the inter-laminar one ( $G_{dc}$ ) can be tuned such that  $\rho^{10}$  emerges, leading to  $G_{dc}^{10} = 0.45 \cdot G_{mc}^{10}$  (see Fig. 17). As it can be seen, during the first de-moistening, micro-cracking is the preferred damage mechanism. Since now all parameters are determined, the behavior of other thicknesses can be calculated (Fig. 17). The predicted evolution of the micro-crack density is given in Fig. 17, showing that for an identical moisture change in  $\Delta\omega = 20 \%$ , the resulting crack density for  $d = 20 \text{ mm}$  is  $\rho^{20} = 0.02 \text{ mm}^{-1}$ , which

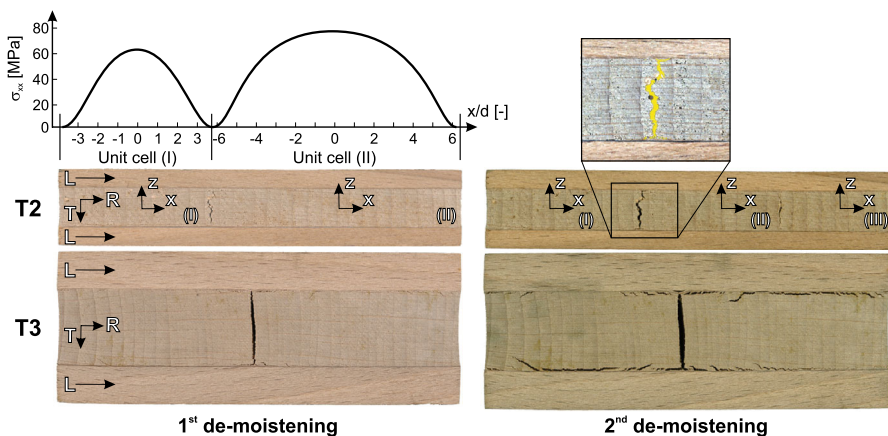


**Fig. 16** Side views of the fractured and delaminated P2-PUR-T2-1/T3-3 samples after the first and the second de-moistening. The detail shows the micro-crack-induced delaminations emanating from the micro-crack tips after the second drying.  $\sigma_{xx}$  is the average tensile stress along the  $x$ -direction in the middle lamella, from the analytical solution (Nairn and Hu 1994)

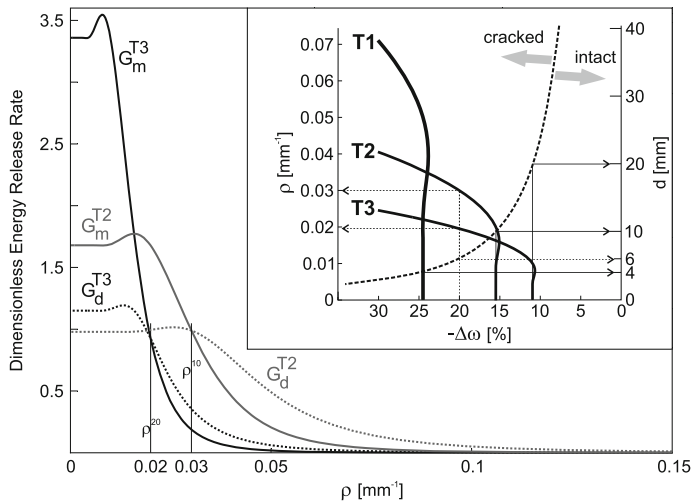


**Fig. 17** Dimensionless ERR versus micro-crack density fitted to T2 and applied to T3 samples, giving excellent agreement with the experimental observations. *Inset* micro-crack density as a function of moisture gradient for P2-PUR-T1/T2/T3 samples and the limit line for micro-cracking initiation

is in agreement with the experiments (see Fig. 10). As a matter of fact, the accurate equilibrium critical inter-laminar ERR can be obtained as  $G_{dc}^{20} = 0.71 \cdot G_{mc}^{10}$ , which is close to  $G_{dc}^{10}$  considering the finite size of the samples. It also becomes evident that the threshold for micro-cracking is not reached for T1 samples. When all critical moisture changes for the onset of micro-cracking are plotted as a function of thickness, the critical thickness for  $\Delta\omega = 20\%$  is extracted to be about  $d = 6$  mm, which is presented in Fig. 17 inset as the limit line (bold dashed line).

Micro-mechanics of damage is a simple 2D approach and cannot capture the effect of the third direction. Considering the simplified material behavior and the limited dimensions of the samples, the predictability of the model and its quantitative agreement is surprisingly good. However, the obtained critical ERR are strongly dependent on the anatomic orientations which should be considered in a study with broader experimental basis.

## Conclusion

The current work demonstrated that delamination of hardwood bonding as well as fracture of hardwood adherends under changing climate can be studied on configurations and also under conditions that are much closer to real applications than typical delamination tests like the DIN EN 14080 (2013) for hardwood. In a combined experimental and numerical investigation, three-layered European beech panels of aligned and crosswise configurations adhesively bonded with the MUF/PRF/PUR were subjected to cyclic climatic variations. In this study, the aim was set on covering a large parameter space, which led to a larger scatter of results by

nature. Similar to the tensile-shear tests, the scatter can be drastically reduced by a careful selection of samples. Note that all adhesive bonds were produced in a moist condition, outside the specifications of the respective adhesives, to obtain more severe crack and delamination states. Consequently, MUF bond lines showed predominant adhesive failure compared to PRF/PUR adhesive joints with predominant interphase failure. This distinction originates from the superior performance of the PRF/PUR adhesive systems exhibiting larger fracture toughness than the respective solid wood substrates.

Furthermore, it was indicated that due to high moisture gradients across the bond line (see Fig. 11), resulting from the noticeable vapor resistance of the adhesive systems used, significant inelastic deformations and consequently local stresses build up under moisture cycling that lead to inter- and intra-laminar damage. By performing 3D moisture-stress FE calculations with elaborated wood and adhesive material models, changes in the strain field in the region of the crack tips that are important for delamination initiation were captured. Moreover, it was demonstrated how the viscoelastic and mechano-sorptive strains relax upon formation of transverse cracks in the middle layer, how the plastic strains build up, and how the strain evolution in the moist states determines the stress situation upon drying, where crack initiation is observed in practice (see Fig. 12). The potential of stress dissipation within bond lines to avoid delamination initiation was illustrated by calculating identical situations with different adhesive material models. Numerical simulation of interfacial delamination under de-moistening was also carried out using the cohesive interface elements within the context of nonlinear fracture mechanics.

In addition, it was shown within a certain range of the middle layer thickness  $d \leq 20$  mm, how an adopted micro-mechanics of damage approach can be applied, for comparable growth ring orientations. This provides limit thickness values for the onset of micro-cracking (see Fig. 17) and the values of adhesive bond line delamination ratios (see Fig. 10) under conditions similar to practical situations. This approach can be directly utilized by producers of cross-laminated timber (CLT) and veneer plywood to calculate the range of application of specific laminates for climatic changes.

It is believed that the proposed computational model has a large potential for optimizing homogenous and even hybrid CLT configurations with respect to the composition (lamella orientation and thickness) and other process parameters such as moisture differences among lamellae.

**Acknowledgments** This work was funded by the Swiss National Science Foundation in the National Research Programme NRP 66—Resource Wood under Grant No. 406640-140002: Reliable timber and innovative wood products for structures.

## References

- ABAQUS (2014) ABAQUS Documentation v. 6.14. Simulia. © Dassault Systèmes
- Alfano G, Crisfield MA (2001) Finite element interface models for the delamination analysis of laminated composites: mechanical and computational issues. *Int J Numer Methods Eng* 50(7):1701–1736

- Ammann S, Schlegel S, Beyer M, Jung H, Niemz P (2016) Quality assessment of glued ash wood for construction engineering. *Eur J Wood Prod* 74:67–74
- de Borst R, Gutiérrez MA, Wells GN, Remmers JJC, Askes H (2004) Cohesive-zone models, higher-order continuum theories and reliability methods for computational failure analysis. *Int J Numer Methods Eng* 60(1):289–315
- DIN EN 14080 (2013) Timber structures: glued laminated timber and glued solid timber: requirements; German version, DIN German Institute for Standardization
- Fortino S, Mirianon F, Toratti T (2009) A 3D moisture-stress FEM analysis for time dependent problems in timber structures. *Mech Time-Depend Mater* 13(4):333–356
- Fortino S, Zagari G, Mendicino AL, Dill-Langer G (2012) A simple approach for FEM simulation of Mode I cohesive crack growth in glued laminated timber under short-term loading. *J Struct Mech* 45(1):1–20
- Gereke T (2009) Moisture-induced stresses in cross-laminated wood panels. PhD thesis, ETH Zurich
- Hass P, Wittel FK, McDonald SA, Marone F, Stampanoni M, Herrmann HJ, Niemz P (2010) Pore space analysis of beech wood: the vessel network. *Holzforschung* 64(5):639–644
- Hass P, Mendoza M, Wittel FK, Niemz P, Herrmann HJ (2012a) Inverse determination of effective mechanical properties of adhesive bondlines. *Eur J Wood Prod* 70:785–790
- Hass P, Wittel FK, Mendoza M, Herrmann HJ, Niemz P (2012b) Adhesive penetration in Beech wood. *Wood Sci Technol* 46(1–3):243–256
- Hass P, Wittel FK, Niemz P, Herrmann HJ (2013) Generic failure mechanisms in adhesive bonds. *Holzforschung* 67(2):207–215
- Hassani MM, Wittel FK, Hering S, Herrmann HJ (2015) Rheological model for wood. *Comput Methods Appl Mech* 283:1032–1060
- He MY, Evans AG, Hutchinson JW (1994) Crack deflection at an interface between dissimilar elastic materials: role of residual stresses. *Int J Solids Struct* 31(24):3443–3455
- Hering S (2011) Characterization and modeling of material properties of beech wood for simulation of glued-laminated wood, PhD Thesis ETH No. 19903
- Kläusler O, Clauß S, Lübke L, Trachsel J, Niemz P (2013) Influence of moisture on stress–strain behaviour of adhesives used for structural bonding of wood. *Int J Adhes Adhes* 44:57–65
- Liu S, Nairn JA (1990) Fracture mechanics analysis of composite microcracking: experimental results in fatigue. In: Proceedings of the 5th technical conference on composite materials american society of composites, East Lansing, Michigan, June 11–14, pp 287–295
- Mendoza M, Hass P, Wittel FK, Niemz P, Herrmann HJ (2012) Adhesive penetration of hardwood: a generic penetration model. *Wood Sci Technol* 46(1–3):529–549
- Nairn JA (1989) The strain energy release rate of composite microcracking: a variational approach. *J Compos Mater* 23(11):1106–1129
- Nairn JA, Hu S (1992) The initiation and growth of delaminations induced by matrix microcracks in laminated composites. *Int J Fract* 57(1):1–24
- Nairn JA, Hu S (1994) Micromechanics of damage: a case study of matrix microcracking. In: Talreja R (ed) *Damage mechanics of composite materials* (Chapter 6), composite material series 9. Elsevier Science, Amsterdam, pp 187–243
- Qiu LP, Zhu EC, van de Kuilen JWG (2014) Modeling crack propagation in wood by extended finite element method. *Eur J Wood Prod* 72(2):273–283
- River BH (2003) Fracture of adhesive-bonded wood joints. In: Pizzi A, Mittal KL (eds) *Handbook of adhesive technology*, revised and expanded, 2nd edn. Taylor & Francis, London
- Serrano E (2000) Adhesive joints in timber engineering: modelling and testing of fracture properties. Technical report TVSM-1012, PhD thesis Lund University
- Serrano E (2004) A numerical study of the shear-strength-predicting capabilities of test specimens for wood–adhesive bonds. *Int J Adhes Adhes* 24(1):23–35
- Silva M, de Moura M, Morais J (2006) Numerical analysis of the ENF test for mode II wood fracture. *Compos Part A-Appl S* 37(9):1334–1344
- Simon F, Valentin G (2003) Cohesive failure characterisation of wood adhesive joints loaded in shear. *ESIS Publ* 32:305–316
- Touati D, Cederbaum G (1997a) Stress relaxation of nonlinear thermoviscoelastic materials predicted from known creep. *Mech Time-Depend Mater* 1(3):321–330
- Touati D, Cederbaum G (1997b) On the prediction of stress relaxation from known creep of nonlinear materials. *J Eng Mater Technol* 119(2):121–124



- Volkmer T, Schmidt JA, Kranitz K, Niemz P (2012) Studies on the influence of the type of adhesive on the diffusion resistance of wood adhesives. *Bauphysik* 34(2):55–60
- Wimmer R, Kläusler O, Niemz P (2013) Water sorption mechanisms of commercial wood adhesive films. *Wood Sci Technol* 47(4):763–775
- Wittel FK, Kun F, Kröplin BH, Herrmann HJ (2003) A study of transverse ply cracking using a discrete element method. *Comput Mater Sci* 28(3–4):608–619
- Wittel FK, Dill-Langer G, Kröplin BH (2005) Modeling of damage evolution in soft-wood perpendicular to grain by means of a discrete element approach. *Comput Mater Sci* 32(3–4):594–603
- Zhang X, et al (2005) Comprehensive hygro-thermo-mechanical modeling and testing of stacked die BGA module with molded underfill. In: *Proceedings of the 55th electronic components and technology conference* (Lake Buena Vista, FL) 1:196–200